Tellus (1997), 49A, 277–297
Printed in UK – all rights reserved

TELLUS
ISSN 0280–6495

Satellite observation and climate system model simulation of the St. Lawrence Island polynya

By AMANDA H. LYNCH[1], MARY F. GLUECK[2], WILLIAM L. CHAPMAN[3], DAVID A. BAILEY[4] and JOHN E. WALSH[3] [1]*Antarctic CRC, University of Tasmania, Hobart, Tasmania, Australia,* [2]*Laboratory for Tree-Ring Research, University of Arizona, Tucson, Arizona, USA;* [3]*Department of Atmospheric Sciences, University of Illinois, Urbana, Illinois, USA;* [4]*Geophysical Institute, University of Alaska, Fairbanks, Alaska, USA*

(Manuscript received 29 August 1995; in final form 6 September 1996

ABSTRACT

The St. Lawrence Island polynya (SLIP) is a commonly occurring winter phenomenon in the Bering Sea, in which dense saline water produced during new ice formation is thought to flow northward through the Bering Strait to help maintain the Arctic Ocean halocline. Winter darkness and inclement weather conditions have made continuous in situ and remote observation of this polynya difficult. However, imagery acquired from the European Space Agency ERS-1 Synthetic Aperture Radar (SAR) has allowed observation of the St. Lawrence Island polynya using both the imagery and derived ice displacement products. With the development of ARCSyM, a high resolution regional model of the Arctic atmosphere/sea ice system, simulation of the SLIP in a climate model is now possible. Intercomparisons between remotely sensed products and simulations can lead to additional insight into the SLIP formation process. Low resolution SAR, SSM/I and AVHRR infrared imagery for the St. Lawrence Island region are compared with the results of a model simulation for the period of 24–27 February 1992. The imagery illustrates a polynya event (polynya opening). With the northerly winds strong and consistent over several days, the coupled model captures the SLIP event with moderate accuracy. However, the introduction of a stability dependent atmosphere-ice drag coefficient, which allows feedbacks between atmospheric stability, open water, and air-ice drag, produces a more accurate simulation of the SLIP in comparison to satellite imagery. Model experiments show that the polynya event is forced primarily by changes in atmospheric circulation followed by persistent favorable conditions: ocean surface currents are found to have a small but positive impact on the simulation which is enhanced when wind forcing is weak or variable.

1. Introduction

The Bering Sea region (Fig. 1a) is the only direct oceanic link between the Arctic and Pacific Oceans. The broad, shallow northeastern shelf region of the Bering Sea is unique in the Western Arctic in that it is ice-covered in winter but completely ice free in summer. In general, the sea ice observed in the Bering Sea is first-year ice with thicknesses of 0.01 to 1.0 m. Ice is primarily formed within the basin and advected southward in a conveyor belt fashion (Pease, 1980) rather than entering from the Bering Strait region. The ice forms and drifts southward, driven by the prevailing northerly winds (Overland and Pease, 1982). Winds are considered to be the primary forcing mechanism for sea ice drift and polynya development in the Bering Sea, since the observed mean flow of water over the shelf is only 0.01–0.03 ms^{-1} towards the northwest (Schumacher et al., 1983). Maximum ice extent is generally reached

* Corresponding author.

by April. At the end of the season, ice retreat occurs through in situ melting and, to a lesser extent, via northward drift, until no ice remains south of the Bering Strait in late June.

Polynyas (recurring openings in the ice cover) are sites of localized high rates of heat and moisture exchange between atmosphere and ocean (Martin and Cavalieri, 1989), as well as locations of high rates of ice production. Further, the regular occurrence of polynyas in the seasonal sea ice zone represents an important source of dense saline water for the maintenance of the Arctic Ocean halocline, which in turn plays a major role in the Arctic ocean-atmosphere heat exchange processes by limiting vertical heat transport (Aagaard et al., 1981). As polynyas are common (Maykut, 1982; McNutt, 1981) it is crucial to represent the dynamic and thermodynamic processes of polynya formation in climate models in order to achieve a realistic simulation of the ocean-ice-atmosphere feedbacks in the Arctic.

The St. Lawrence Island polynya (SLIP) occurs at least once each year in the Bering Sea during the winter season. St. Lawrence Island (Fig. 1b), located just south of the Bering Strait, is bounded on the west by a branch of the Anadyr current and on the east by the weak current through Shpanberg Strait. The waters surrounding the island combine with the Alaska coastal current and the strong Anadyr Current as they flow north through the Bering Strait into the Arctic Ocean (Schumacher et al., 1983; Overland and Roach, 1987). Currents near St. Lawrence Island are 0.02–0.08 ms^{-1}, but these currents can be baroclinically enhanced to 0.10 ms^{-1} during polynya events due to the effect of brine rejection on the local density structure (Schumacher et al., 1983). The southern coast of St. Lawrence Island is approximately 270 km long with two shallow bay areas. The SLIP (Fig. 4) is a wind-generated winter feature which opens up along the southern coast during periods of sustained northerly winds. Open water and newly formed ice can exist along the entire southern coastline, with polynya events generally lasting from 3 to 10 days. Other wind-driven Bering Sea polynyas exist off the coasts of St. Matthew Island and Nunivak Island, and along the lee coasts of Siberia and Alaska.

Satellite observations of the polynyas have previously been limited to large-scale, low resolution satellite imagery or costly field expeditions both of which are highly dependent on season and cloud conditions (Carsey, 1989). The recently launched European Space Agency (ESA) Earth Remote Sensing Satellite 1 (ERS-1) which carries a Synthetic Aperture Radar (SAR) has made a new form of high spatial (240 m) and temporal (three day repeat) resolution imagery available for use. As the SAR is an active C-band microwave instrument, it is unaffected by darkness, or by the dense cloud cover which tends to be prevalent during Bering Sea winters. The resulting SAR imagery can also be processed to create ice motion products. Further, SAR imagery can be combined with other remote sensing products (e.g., surface temperature from AVHRR* and ice concentration from SSM/I** to produce a comprehensive picture of the ice circulation and the process of polynya formation.

Modeling a SLIP event (the opening of the polynya) has been a difficult task due to the relatively small size of the polynya, (Pease, 1987). Global climate model grid sizes of 200–400 km, for example, are much larger than the polynya, and smaller scale process models do not allow the complex feedbacks which take place between ice, atmosphere and ocean. With the development of the Arctic Region Climate System Model (ARCSyM), a high resolution model of the Arctic climate system (Lynch et al., 1995), it is now possible to simulate the polynya formation process with minimal external forcing. The use of the newly-acquired remote sensing products can now be extended further to model comparison in addition to observation of the polynya event. Section 2 describes the data and Section 3 describes the model used for this study. In Section 4, a detailed analysis of the SLIP event of February 1992, both observed and simulated, is presented.

The drag coefficient is one of the most important parameters in modeling ice motion for the purposes of regional climate simulations, since the surface wind is the principal forcing mechanism for ice drift (Thorndike and Colony, 1982). Thus, the response of the model to changing formulations of the drag coefficient, including its dependence on stability and ice type, is examined in Section 5. The role of the oceanic circulation is

* Advanced Very High Resolution Radiometer, NOAA 11 and NOAA 12.

** Special Sensor Microwave/Imager.

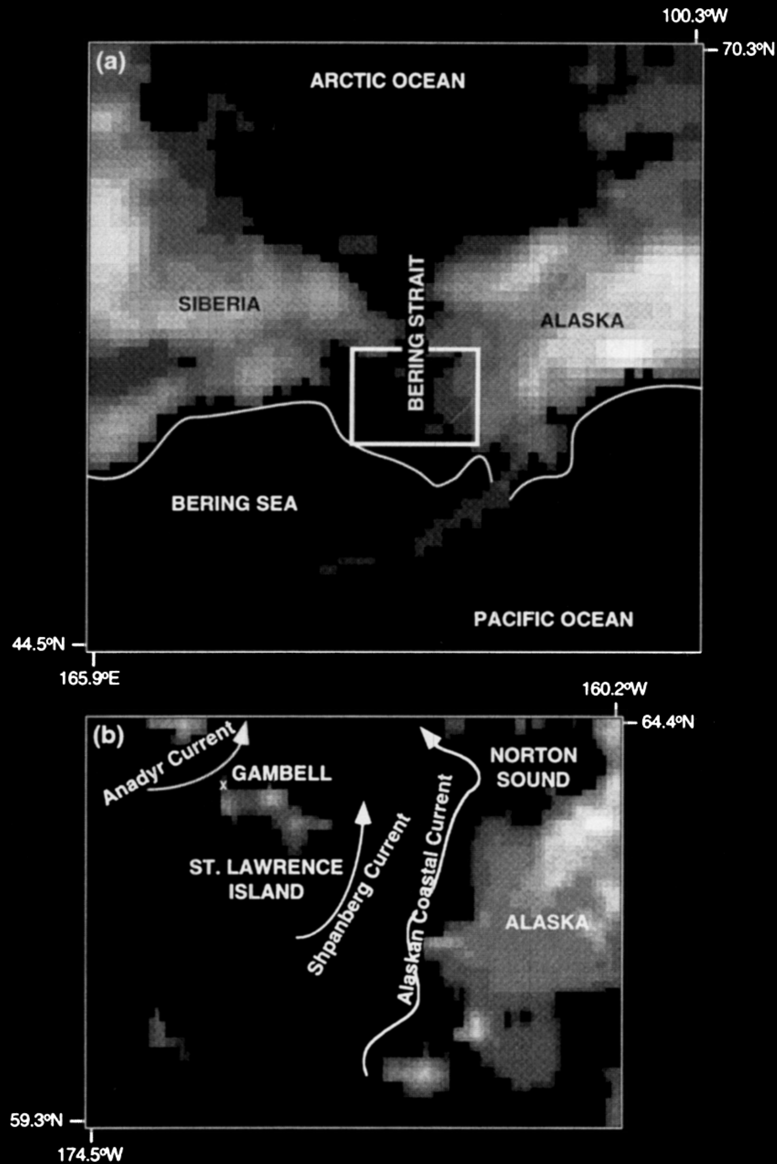

Fig. 1. (a) Map of area of interest, showing Alaska, Siberia, and the Bering Strait. Also shown is the ice edge for 24 February based on SSM/I imagery. The box indicates the numerical model domain used in these experiments. (b) The model domain, showing St. Lawrence Island and Gambell, the meteorological station on St. Lawrence Island.

considered by including forcing by ocean currents derived from a barotropic model, with a comparison between the SLIP event examined in detail and a later period characterized by weak and variable forcing; the results are discussed in Section 6.

While prediction is a goal of any model experiment, a climate system model can go beyond this to investigate complex feedback mechanisms as well as isolated processes. There have been many other studies carried out in this region involving analytic models (Pease, 1987), observations

(Schumacher et al., 1983), satellite (Massom and Comiso, 1994), atmosphere-ice relationships (Niebauer, 1980), and many others too numerous to cover here. This study is a logical next step for all of these, using newly acquired satellite imagery and imagery-based ice motion products, along with a coupled climate model that has the potential to indicate the effect of this region on the Arctic climate system as a whole.

2. Data

2.1 Satellite data

Sea ice data were obtained from low resolution (LoRes) ERS-1 SAR imagery and Geophysical Processor System (GPS) ice motion products, SSM/I ice concentration and classification products, and AVHRR imagery (Band 4 Thermal IR). The combination of satellite data from several sources allowed a more comprehensive picture of the SLIP to be produced. It is the use of ice motion products in conjunction with satellite imagery to verify a climate system model which is an original contribution of the present study.

Detailed descriptions of basic synthetic aperture radar theory and image processing/interpretation procedures applicable to sea ice analyses are available (Ulaby, 1981; McCandless and Mango, 1990; Curlander, 1985; Carsey, 1992), and hence only a brief description will be presented here. The ERS-1 SAR is an active C-band microwave ($\lambda = 5.6$ cm) single channel radar. SAR images are constructed from Doppler phase histories stored in the radar return signal. Because the SAR is a microwave sensor, it can operate during any light conditions and can penetrate cloud cover, making it an ideal sensor for seasonal sea ice applications.

LoRes SAR imagery (100 km $\times$ 100 km images, pixel size 100 m) for the St. Lawrence Island area were obtained from the 1991/1992 ice phase orbit* archive at the Alaska SAR Facility on a three-day repeat cycle (DeSoto et al., 1991). The SAR imagery was radiometrically-corrected (backscatter normalized to a defined scale) and combined into mosaic image strips for each date. Imagery used in this project covered the period from 18 February to 1 March 1992.

* A sun-synchronous orbit alignment specifically designed for sea ice observation.

Ice motion products are produced using selected pairs of consecutive, geocoded (geographically registered) LoRes SAR imagery through a combination of feature-based and area-based methods of tracking ice floes (Kwok et al., 1991). This set of motion products was produced on the Geophysical Processor System (GPS) associated with the ERS-1 SAR program at the NASA Jet Propulsion Laboratory (Kwok, personal communication). The ice displacement techniques attempt to incorporate both the rotational and translational motion taking place between satellite passes. Initial co-location of ice features is based on estimates of short-term ice drift from geostrophic wind/ice relationships (Thorndike and Colony, 1982). Feature tracking is then attempted by correlating distinct features such as pixel intensity, floe shape, or other similar attributes. The area matching stage is initialized by the feature matching results. Area matching takes advantage of the geographic mapping (SSM/I grid) of the image by checking all possible feature matches within a pre-specified window or patch centered at a grid point. The best matches are determined using FFT and cross correlation techniques. A set of displacement values of the best matched features constitutes an ice motion product associated with each SAR image pair.

Due to the rapid and highly divergent nature of the ice motion, the SLIP vector products required non-standard processing with extensive visual inspection to obtain a high quality dataset. Although the resulting vectors are acceptable, it was evident that some limitations remain. Poor detection and tracking of features was noted where ice was thinnest and drifting rapidly within the polynya region itself. Further, there was great variability in the number of points which could be paired in consecutive images. In general, validation error statistics for GPS ice motion products show an initial uncertainty in geolocation of common features to be 100–200 m due to errors inherent in the geographic registration of the imagery (Kwok and Cunningham, 1993), while motion errors are thought to be 300 m over three days (Stern, personal communication). In this case, the ice motion errors are likely to be higher due to the highly dynamic nature of the ice motion in the region, but are within the 7 km grid cell size of the model (see Section 3).

AVHRR imagery were obtained from NESDIS

(National Environmental Satellite Data and Information Service) and from the National Weather Service Forecast Office Anchorage. The AVHRR thermal infrared band (Band 4) was calibrated for temperature and geo-registered to the stereo-polargraphic map projection of the SAR imagery. The AVHRR pixel size (1.1 km) was then re-scaled to match that of the SAR imagery. Finally, the imagery were color-mapped to represent surface temperatures based on ice type boundaries visible in the SAR imagery. This was necessary as newly formed ice and open water have similar backscatter values during windy periods making distinct boundaries difficult to determine with SAR alone.

While the synoptic coverage of AVHRR imagery is excellent, image interpretation of sea ice is greatly hampered by the presence of clouds, which are often similar in temperature to the ice. Further, the detrimental effects of atmospheric constituents such as water vapor, even in the absence of clouds, must be considered. Although many cloud masking, atmospheric filtering and sea ice extraction methods exist (Key and Haefliger, 1992; Haefliger et al., 1993; Maslanik and Key, 1993; Massom and Comiso, 1994) there are no established procedures for filtering clouds and atmospheric effects in thermal IR data acquired during winter dark periods. The use of unfiltered Band 4 data is an acceptable alternative (McMillan and Crosby, 1984) since atmospheric water vapor contamination is smallest at the Band 4 wavelengths. Further, the AVHRR imagery used here were chosen for their minimal cloud cover.

Daily brightness temperature data were obtained from CD-ROMs created by NSIDC (National Snow and Ice Data Center, Boulder; NSIDC, 1992). Brightness temperatures were obtained from DMSP (Defense Meteorological Satellite Program) F11 satellite SSM/I (passive microwave) data. The NASA Team algorithm (Cavalieri et al., 1984 and 1991; Gloersen and Cavalieri, 1986) was applied to the brightness data to obtain daily ice concentration fields for our study period. Although ice concentration derived using this algorithm is known to be in error by at least 10% (Gloersen et al., 1992), it was considered to be the best ice concentration data available for this region. Daily ice concentration values were obtained for first-year ice, multi-year ice, and a combined or composite field. As this region of the Bering Sea rarely contains multi-year ice, only the first-year ice fields were used in our study.

2.2 *Atmospheric observational analyses*

Atmospheric data for the period were obtained from ECMWF* analyses (Trenberth, 1992), which are produced using four dimensional data assimilation. These data provide the initial and lateral boundary conditions for the model simulations, as well as a means of broad scale model verification. The archive, obtained from NCAR**, consists of 6-hourly analyses on 14 pressure levels, using a T42 truncation from the ECMWF T106 spherical harmonics. The archived fields include geopotential, temperature, wind, humidity, surface pressure and orography.

3. Model description

The ARCSyM has been described in detail in Lynch et al. (1995); only a brief summary of the relevant details will be reproduced here. The model is based on the NCAR RegCM2 (Giorgi et al., 1993a), a hydrostatic, primitive equation model with a terrain following vertical coordinate (sigma coordinate) and a staggered "Arakawa B" horizontal grid. The model incorporates the land surface exchange and vegetation model BATS1E (Biosphere-Atmosphere Transfer Scheme Version 1E, Dickinson et al., 1993) and the CCM2 radiative transfer scheme (Briegleb, 1992a, 1992b) and a dynamic/thermodynamic sea ice model. The physical parameterizations used in ARCSyM are shown in Table 1.

The sea ice model is based on the cavitating fluid ice dynamics scheme of Flato and Hibler (1992) with the anti-diffusion option and the thermodynamics of Parkinson and Washington (1979). The cavitating fluid rheology was chosen to parameterize the internal ice stress because it has been shown to be computationally efficient and stable at higher resolutions. The cavitating fluid formulation assumes that the pack ice is a two-phase medium in which the open water phase has no strength at all while the ice phase is

* European Centre for Medium Range Weather Forecasting.

** National Center for Atmospheric Research.

Table 1. *Physical parameterizations used in the atmospheric module of ARCSyM*

Physical process	Model treatment
horizontal diffusion	same as NCAR/PSU MM4 (Anthes et al. 1987) but with diffusivity reduced in the presence of topographical gradients so as to minimize spurious diffusion of moisture and temperature in those regions.
radiative transfer	CCM2 radiation scheme (Briegleb 1992a, 1992b)
boundary layer physics	explicit PBL scheme of Holtslag et al., (1990)
land hydrology	BATS1E (Dickinson et al. 1993)
cumulus cloud processes	one-cloud scheme of Grell (1993)
grid scale moist processes	explicit scheme (Hsie et al. 1984)
lateral boundary conditions	exponential relaxation (Giorgi et al. 1993b)

relatively rigid. Thus, the composite medium is free to diverge, while it resists compaction due to the rigidity of the ice phase. The ice phase is not completely rigid and hence will compress and thicken until a limiting compressive ice strength is reached. This maximum compressive strength is a function of both the ice thickness and the ice concentration (compactness). The surface drag coefficient is specified for unstable conditions as 0.002 for wind speeds less than 10 ms^{-1}, 0.003 for wind speeds greater than 20 ms^{-1}, and varies linearly for wind speeds between 10 and 20 ms^{-1}, with a reduction for stable conditions. The thermodynamics formulation is a simple two layer model allowing for ice, leads and snow cover. Thermodynamic changes in thickness of the ice and snow layers are based on energy balances at the various interfaces, taking into account the precipitation of snow. The turbulent heat and moisture fluxes are parameterized using the standard bulk aerodynamic formulae, with the turbulent transfer coefficient a function of the near surface atmospheric stability. The bulk Richardson number is calculated separately over ice and open water surfaces as a measure of the stability of the near surface environment (Curry and Ebert, 1992).

The model domain (Fig. 1b) is a region centered south of the Bering Strait. The 7 km horizontal grid resolution is high for a regional model, (compared with the resolution of a standard regional climate model of around 60 km, as shown in Figure 1a, and a standard GCM model resolution, generally above 150 km). This is reaching the upper limit for a hydrostatic model. The model contains 23 σ levels in the vertical, with the highest resolution in the boundary layer. The model was initialized on 18 February 1992 using ECMWF analyses, and a uniform ice cover 1.5 m thick with 99.5% concentration. Initial ice edge data were obtained from the weekly ice concentration charts of the Navy/NOAA Joint Ice Center; snow cover over land and ice was initialized to 0.3 m depth at all grid points that were initially colder than 0°C (all points during this season). Initial sea surface temperatures outside the ice pack were derived from the data of Shea et al. (1992), with modifications for compatibility with observed ice cover. The model control simulation commenced on 18th February and continued for 9 days. Results will be shown following a 6 day spin up of the ice motion for the period 24–27 February.

4. Slip event of February 1992

Polynya formation is possible under favorable conditions at St. Lawrence Island from December to April. In the winter of 1991–1992, the ice reached the island by mid-December. The polynya event focused on here was the second such event of that winter, and a time series of analyzed sea level pressure for the region and simulated ice concentration south of St. Lawrence Island are shown in Fig. 2. On the 18th and 19th of February, a strong low pressure system was located west of the island, but by the 20th weak high pressure dominated the area as a new low developed in the Gulf of Alaska (Fig. 2a). Over the next few days, the area of high pressure was pushed northwestward as the Gulf of Alaska low deepened, resulting in a shift in wind direction over the island from easterly to northerly, and a corresponding drop in regional air temperatures. The development of the polynya was slow and somewhat erratic from the 18th to the 21st (Fig. 2b), due to the unsettled weather conditions.

From 21–25 February, the Gulf of Alaska low became extremely intense (central pressure 962 mb on the 24th), maintaining a strong prevailing north-northeasterly flow across the eastern Bering Sea (Figs. 2a, 3a). The ARCSyM-simulated pressure field for the 24 February is shown in Fig. 3b. Even after 6 days, the atmospheric simulation shows a close correspondence to the observational analyses. However, model winds with maximum speed of 19 ms^{-1} are more intense than the analyzed speed of 14 ms^{-1} over the model domain, and the simulated wind is shifted slightly to the north from the observed. This discrepancy with the forcing can be seen at the boundaries of the simulation domain (Fig. 3b). Following the dissipation of this low, a second low moved into the Gulf from the North Pacific, maintaining the north-northeasterly winds over the St. Lawrence Island for a few more days.

In response to the favorable wind conditions, the SLIP opened considerably, expanding an additional 95 km southward over the three day period despite intense new ice formation (Fig. 2b). The opening of the polynya appears to be more dramatic in the simulation compared to the time series estimated from SSM/I imagery, which is shown with error bars based on the assessment of Gloersen et al. (1992). This is due to several factors: the high ice concentration (99.5%) of the model initialization requires some spin-up time; the low resolution of the SSM/I imagery compared to the model makes averaging over the same region as the simulation only approximate; the SSM/I imagery is always ambiguous around coastlines, causing potentially larger errors than represented by the standard error bars; and most importantly, the ice model defines open water to be ice less than 30 cm thick, giving an artificially low ice concentration, especially in the rapid ice formation phase of polynya development. The large polynya region (area of open water and thin ice surrounded by the seasonal pack ice and the island) can be seen clearly in the SAR (Fig. 4) and AVHRR (Fig. 5c) imagery of February 24th. Although the polynya region is well-defined in the SAR imagery and in the AVHRR imagery, the actual area of open water is small. It is difficult to distinguish between true open water and new ice because windy conditions result in similar SAR backscatter characteristics. The key to distinction between open ocean, first-year ice and multiyear ice in the imagery is the strength of the backscatter. Calm open ocean has a weak backscatter and thus will appear dark in the image. Rough open ocean will be brighter due to stronger surface scattering by ocean waves. Somewhat weak backscatter is also characteristic of newly formed ice and young ice, which may range from as dark as open water to a medium brightness. Multiyear ice (not present in the images used here) has the strongest backscatter and will appear brightest in an image. The images can also include errors due to gain variations, and limitations in the SAR system range and area of illumination. In an attempt to minimize the effects of these errors, and for interpretation purposes, the SAR images used here have been radiometrically-corrected to allow comparisons between images (Kwok et al. 1991). Through the use of an ice classification technique based on SAR and SSM/I data, Cavalieri and Onstott (1992) have estimated ice concentrations to be as low as 80% in the polynya region on February 27.

The SAR image (Fig. 4) and ice type maps based on SSM/I imagery (not shown) for 24 February indicate a gradation of ice types. The open water within the polynya was short-lived as new ice formed almost as soon as the slightly older ice was blown southward away from the coast. The low temperatures and high wind speeds combined to organize the frazil ice, pancake ice and older ice into ice mats, wind rows (light streaks), or areas of block-like features (broken-up ice floes extending from the island south to the first-year ice) within the polynya region. The gradation is evident for over 65 km south of the island coast at this stage. The first-year ice concentration based on SSM/I imagery is shown in Fig. 5a, and the corresponding simulated ice concentration is shown in Fig. 5b for the sub-region of the model domain corresponding to the SAR polynya coverage in Fig. 4. The simulated concentrations are lower than the 80% level in the

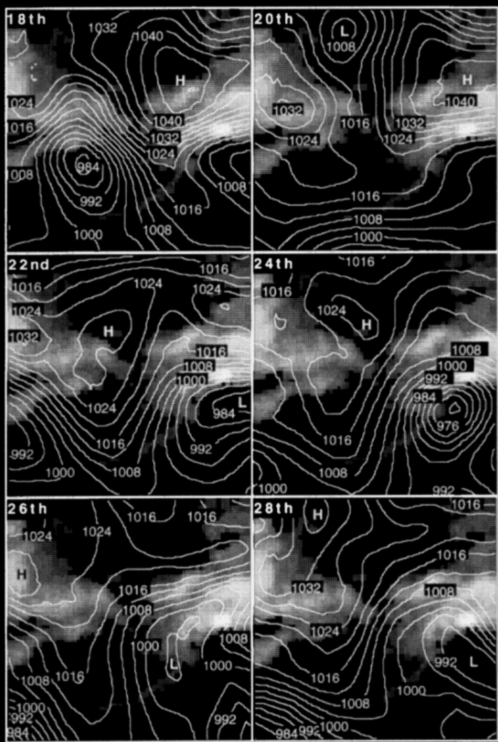

Fig. 2a. Sequence of analyzed sea level pressure for the period 18 February to 1 March 1992 (at 2 day intervals at 00 GMT) to show the progression of systems through the region of interest (Bering Strait, center). Note that the Gulf of Alaska low observed on the 24th to have a central pressure of 962 mb was analyzed to have a central pressure of 972 mb, illustrating the low resolution of the analyses.

polynya, due to the fact that ice thinner than 30cm is defined as open water in the model. Much of the ice in the SLIP is newly formed and well below this thickness level. However, a similar dramatic polynya opening is manifest, with low concentration ice cover extending over 70 km south of the island, although the limitations of the resolution are apparent.

Fig. 5c shows the AVHRR imagery for 16 GMT on the 24th, colored to estimate ice surface temperature, based on ice distributions in the SAR imagery. This data was compared against surface temperatures at Gambell for several time periods and found to be consistently within 2 K of the station observations. St. Lawrence Island is within the gray and black area just above the dark red to dark green banding of the polynya (260–270 K). The area of most intense ice formation is the dark red (>267 K) along the southwest coast of the island. The blue region (257–259 K) is a transitional area of "old" polynya ice (newer than first-year ice), and the gray area surrounding the transitional region to the south, east and west is the seasonal ice pack (<256 K). The simulated surface temperature for the sub-region corresponding to this image is shown in Fig. 5d. While the general distribution of surface temperature corresponds with the AVHRR imagery, the polynya region is on the order of 3 K too warm, and the surrounding seasonal ice pack is around 10 K too cold, resulting in strong horizontal temperature gradients near the edge of the polynya. This indicates the need for a more sophisticated ice thermodynamic formation than the two-layer one currently in use, as well as likely shortcomings in the cloud-radiative interactions (Lynch et al., 1995). In particular, the real polynya is made up of ice in a large range of thicknesses, much of it extremely thin or mixed-phase, whereas the simulated ice is discontinuous in nature, consisting of

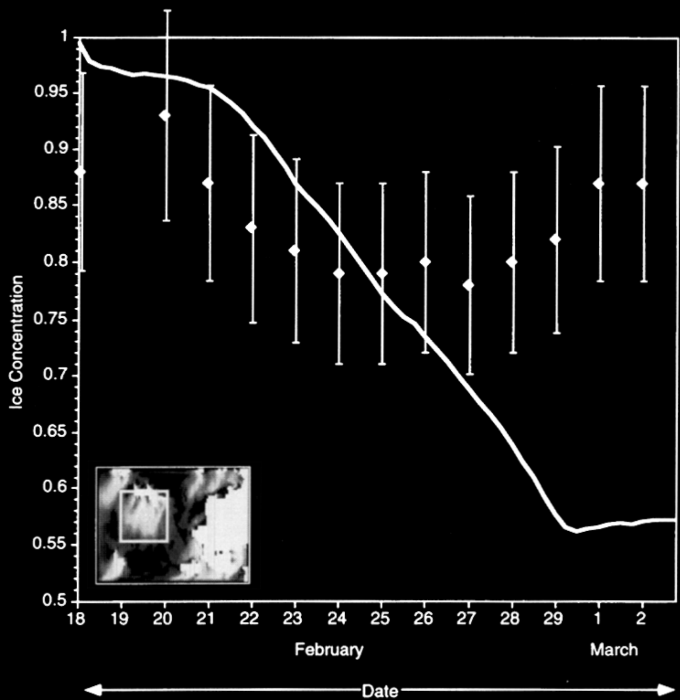

Fig. 2b. Mean simulated ice concentration over the polynya for the period 18 February to 2 March 1992. The mean was taken over the sub-region shown in the cartoon in the bottom left corner of the figure. Also shown is estimated ice concentration over a similar area based on SSM/I imagery, with error bars based on the 10% error estimation of Gloersen et al. (1992). Note that the ice model is initialized with 99.5% ice concentration, requiring a significant spin-up period.

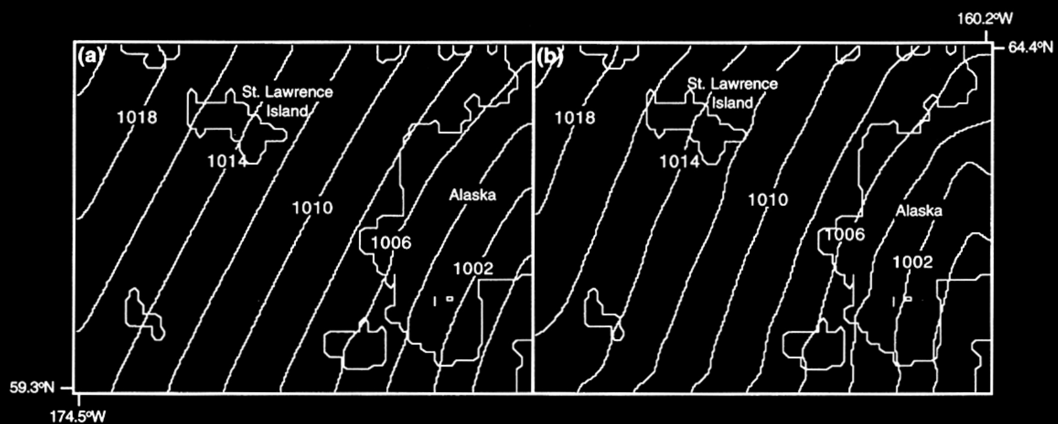

Fig. 3. Mean sea level pressure in hPa at 00 GMT 24 February: (a) ECMWF analysis and (b) model simulation.

open water or ice thicker than 0.3 m. The effect of this simplification can also be seen in the time series comparison of model and SSM/I data in Fig. 2(b). Fig. 6 shows the impact of the polynya throughout the lower layers of the model atmosphere. Shown are temperature and moisture profiles from points upstream, downstream and directly over the polynya. The warming and

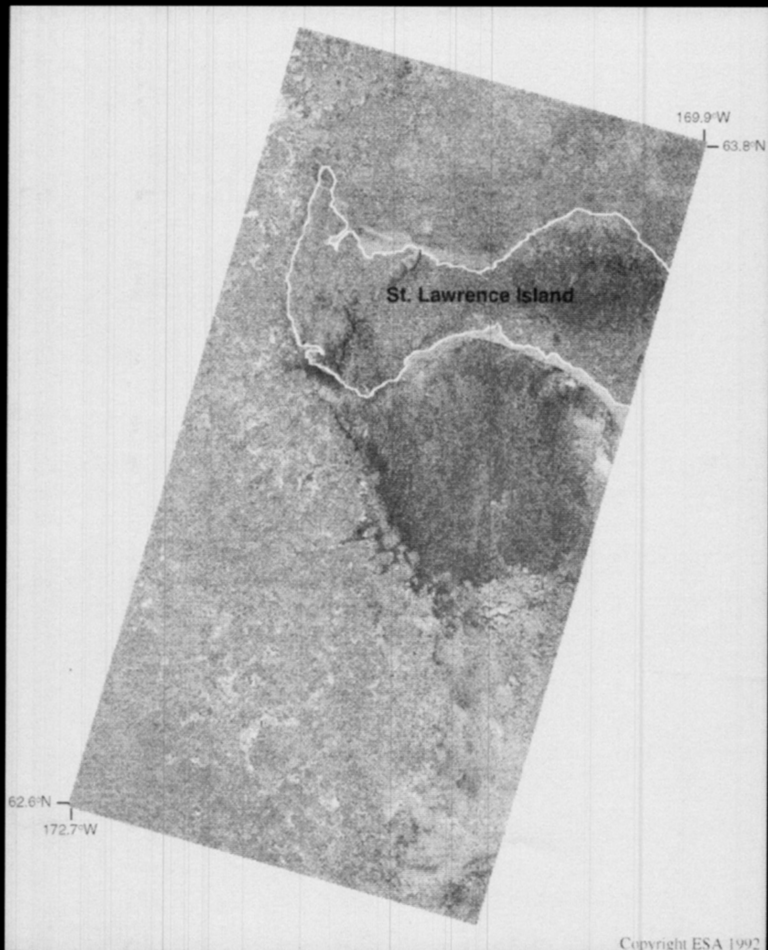

Fig. 4. ERS-1 Synthetic Aperture Radar (SAR) imagery for 22GMT 24 February 1992 (Copyright: ESA 1992). LoRes imagery shows St. Lawrence Island and the St. Lawrence Island polynya (SLIP) which extends southward from the island coast. Backscatter differences are indicative of different ice types and wind conditions. Pixel size is 100 m × 100 m. Imagery is geocoded and radiometrically corrected.

moistening of the atmospheric column above the polynya is clearly defined, with the effect extending as high as the $\sigma = 0.8$ ($\sim$800 mb) level. Further, the effect of the polynya extends many tens of km downstream from the polynya itself. This extended region of impact of the polynya indicates that even if the polynya is too small to be resolved by a GCM, its impact on the atmosphere is potentially of GCM scale, demonstrating the importance of these features as a source of heat and moisture on global scales.

From 24–27 February, winds over St. Lawrence Island averaged 11 ms^{-1} towards the southwest (based on data from the meteorological station at Gambell) resulting in ice motion of 0.33 ms^{-1} ($\sim$3% of the wind speed). The SAR ice motion field is shown in Fig. 7a, with corresponding ice motion vectors simulated by the model over the same time period are shown in Fig. 7b. The simulated ice drift field is interpolated for comparison with *all* available SAR ice drift vectors. The average simulated wind speed over the island was 10.6 ms^{-1} directed towards the southwest. Simulated ice motion indicates ice drifting at 0.35 ms^{-1} (3.3% of the wind speed). The flow of ice around St. Lawrence Island is more conspicuous in the

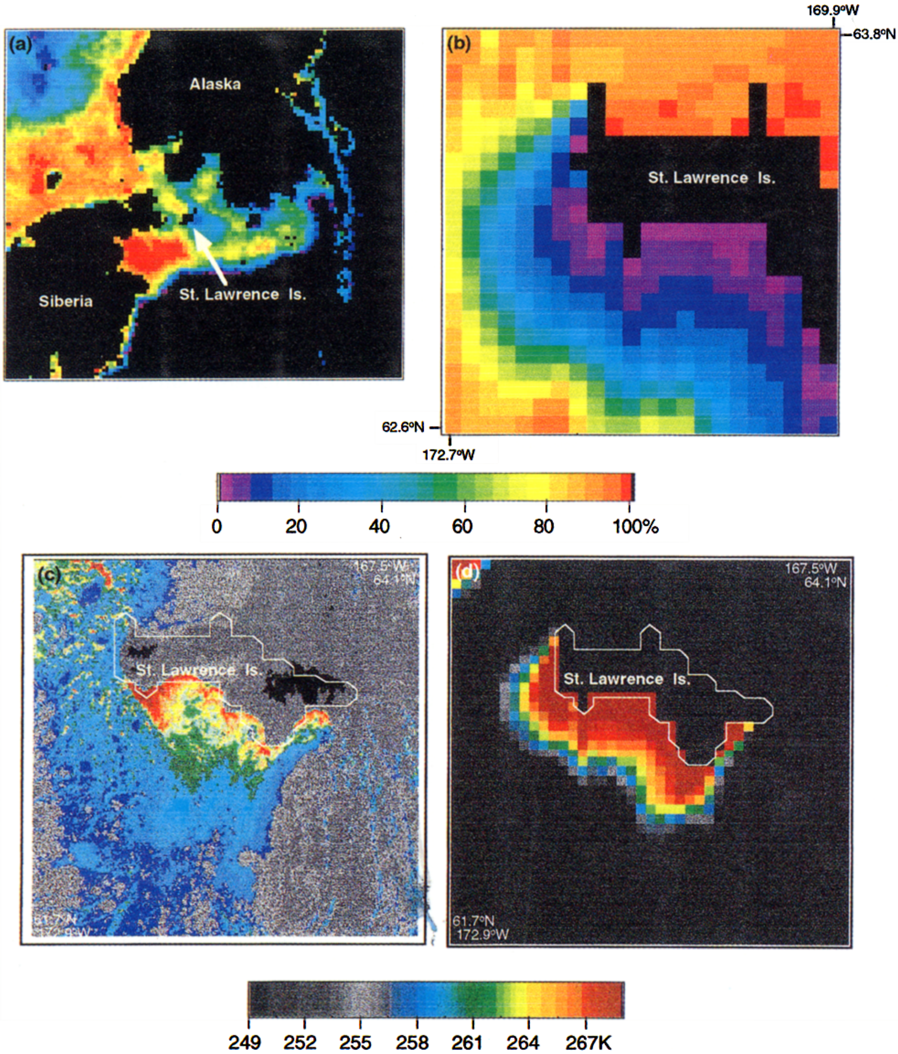

Fig. 5. (a) First-year ice concentration derived from SSM/I brightness temperatures for 25 February 1992. (b) Simulated ice concentration as a percentage for 00 GMT 25 February 1992, for sub-sampled area of model domain to correspond with SAR data in Fig. 4. Pixel size is 7 km × 7 km. (c) NOAA 12 AVHRR Band 4 Thermal Infrared imagery for 1559GMT 24 February 1992. Pixel size is 1.1 km × 1.1 km. Imagery is calibrated, mapped and colored to estimate ice surface temperature, using the color table as shown. Temperature distribution is based on ice spatial variations seen in corresponding SAR imagery. St. Lawrence Island is the gray and black area just above the red to green banding of the polynya. (d) Simulated surface temperature in °K (weighted average of ice and ocean temperatures) for 18GMT 24 February 1992, for sub-sampled area of model domain to correspond with AVHRR data at left. Pixel size is 7 km × 7 km.

model field. This is due to resolution limitations which make St. Lawrence Island appear larger in the simulation. The excellent agreement between simulated and SAR-derived ice motion vectors is due in part to the persistent atmospheric forcing (northeasterly winds) during this period.

The strong northerly flow characteristic of 24–27 February had weakened by 29 February.

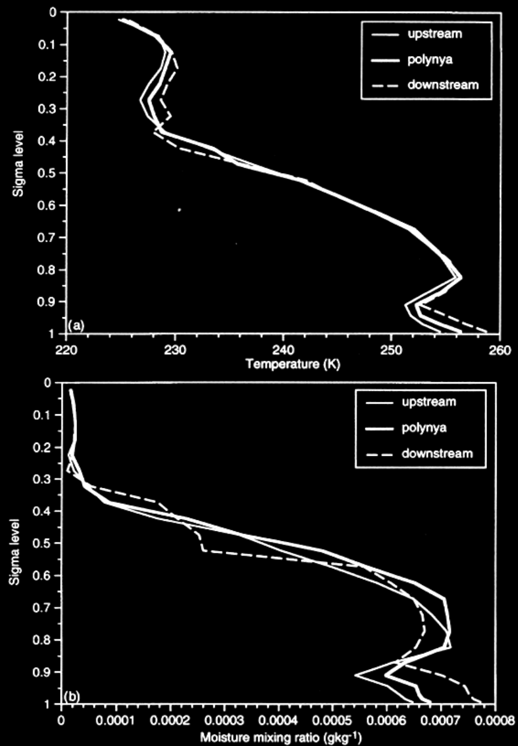

Fig. 6. (a) Temperature (°K) and (b) moisture mixing ratio (gkg^{-1}) profiles for three points situated approximately 50 km upwind of the polynya, directly over the polynya, and approximately 50 km downwind of the polynya.

By this time, the low pressure system in the Gulf of Alaska had moved north and dissipated over land. A second low moved north from the North Pacific into the Gulf of Alaska between the 27–28 February, and then continued to move northward up the west coast of Alaska towards the Chukchi Sea. On 29 February, the low was located directly north of St. Lawrence Island, replacing the prevailing conditions with an extremely weak westerly flow, and the rate of polynya expansion was dramatically decreased.

5. Impact of changing surface drag coefficient

A series of experiments were performed to examine the role of the drag coefficient specification in the ice drift and consequent ice distribution for this case (Table 2). These experiments were initialized from the control experiment on the 22 February and run until the 28 February to capture the impact of the changed drag coefficient in the first period, following the spin up of the sea ice in the model. The first three experiments set the drag coefficient to constant low, medium and high values, respectively, based on the composite data of Overland (1985). Overland attempted to reconcile the broad range of drag coefficients measured over sea ice in aircraft campaigns such as MIZEX (Marginal Ice Zone Experiment; Cavalieri, 1983; Johannessen and Horn, 1984) and AIDJEX (Arctic Ice Dynamics Joint Experiment;

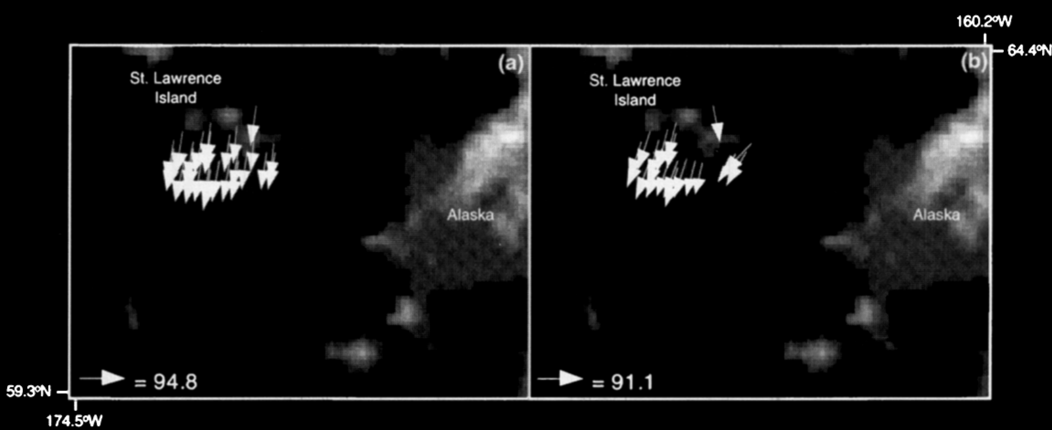

Fig. 7. Ice drift vectors for the period 24–27 February in km per 3 days: (a) derived from SAR imagery and (b) model simulation. Maximum vector for each panel as shown. Vectors are overlaid on a model generated topography field and hence can appear to go through land features due to the low resolution of the model.

Table 2. *Model experiments*

Experiment	Description	Polynya extent at 00 GMT 25 February (SAR estimate: 69 km)
Control	C_D calculated as a simple function of wind speed, with a stability correction of 0.6.	91 km
C10	C_D set to a uniform low value of 1.0×10^{-3}	77 km
C25	C_D set to a uniform medium value of 2.5×10^{-3}	91 km
C40	C_D set to a uniform high value of 4.0×10^{-3}	105 km
CSTAB	C_D is calculated according to Deardorff (1968) as a product of a neutral drag coefficient based on a roughness length of 0.08 m and a stability correction based on the bulk Richardson number.	84 km
CLEAD	C_D is calculated as above but as an area weighted average of the ice and open water drag coefficient.	80 km
CRAFT	C_D is calculated as for CLEAD, but with a correction for low ice concentrations based on Overland's (1985) rafting argument (a correction of 1.3 for ice concentrations below 50%).	80 km
With ocean	ice drift is modified by ocean currents which vary spatially but not temporally.	70 km

Untersteiner, 1980) as well as those obtained from tower measurements. The values found for different conditions in the marginal ice zone and the central Arctic ice pack range from as low as 1.5×10^{-3} to as high as 4×10^{-3}, depending on the combination of floe types and ice concentration. Thus the values for these simulations over the seasonal ice zone were set to 1.0×10^{-3}, 2.5×10^{-3} and 4.0×10^{-3}, in order to address whether ARCSyM's response to drag coefficient variation is linear, or whether there are thresholds involved.

Fig. 8 shows the three day ice drift for 24–27 February for the 3 values of the drag coefficient. The maximum ice drift for the C10, C25 and C40 experiments was 68 km, 115 km and 151 km, respectively, which represents a linear variation of maximum ice drift in this range of drag coefficients. It is clear from these experiments that it is possible to tune the drag coefficient to produce a polynya of the observed north-south extent. There appears to be a direct, almost linear, relationship between a single specified drag coefficient for the whole model domain, and the extent of the resulting simulated polynya. Thus, in theory, one could calculate the appropriate constant drag coefficient for the whole domain to produce the exact extent of polynya desired (Table 2). However, this of course has no physical basis and would not be applicable to other situations and other times—thus illustrating one of the dangers of choosing a single air-ice drag coefficient for the modeling of polynyas.

The second three experiments address the question of a more appropriate drag coefficient calculation than the one presently in use. Overland (1985) found that there was no systematic variation of drag coefficient with wind speed, and suggested that such findings of other authors (e.g. Macklin, 1983) could be explained by the nonlocal effects of upstream roughness. However, it is clear that there are feedback effects between the drag coefficient and the formation of the polynya. As the polynya forms, the surface roughness changes due to the creation of open water and new ice in place of seasonal ice, and ice convergence near the edge of the polynya could cause rafting, and hence increased drag. Furthermore, there is impact upon the stability of the atmospheric profile over the polynya and downstream from it (as shown in Fig. 6): the low level warming and moistening tends to decrease the atmospheric stability and

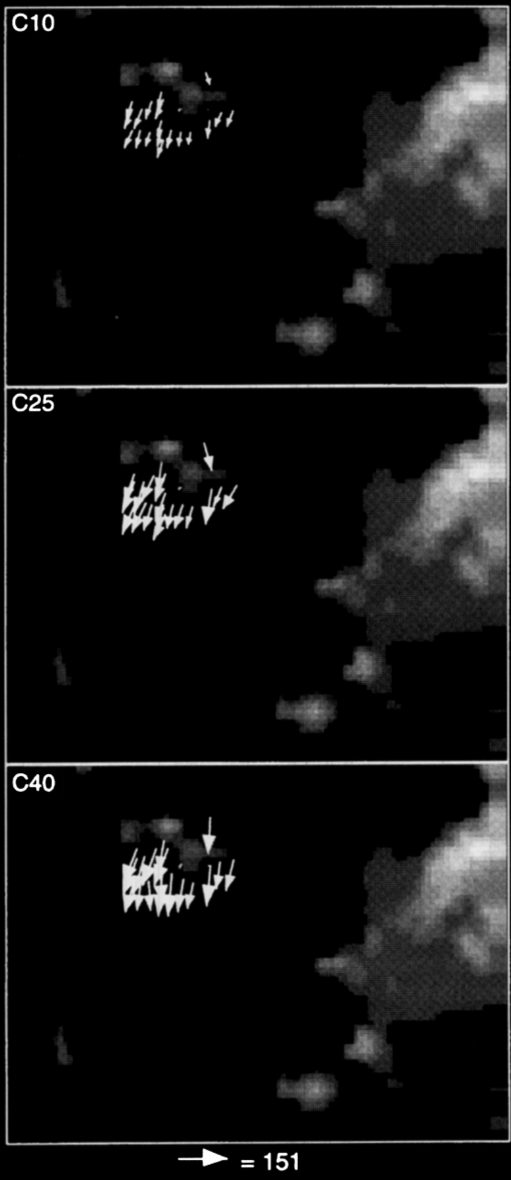

Fig. 8. Ice drift vectors for the period 24–27 February in km per 3 days for the 3 fixed drag coefficient experiments, in which C_d is set to 1.0×10^{-3}, 2.5×10^{-3} and 4.0×10^{-3}, respectively. Maximum drift vector for the three panels is 151 km in 3 days. Vectors are overlaid on a model generated topography field and hence can appear to go through land features due to the low resolution of the model.

hence increase drag. Thus, formulations of the drag coefficient calculation which do not depend simply on wind speed, but do depend on other factors such as surface type and stability, were tested. The stability dependent formulation of Deardorff (1968) was chosen, in which a neutral drag coefficient based on a roughness length is combined with a bulk Richardson number formulation to model the departure of the drag coefficient from its neutral value. The first experiment simply calculates this stability dependent drag coefficient over ice (CSTAB, Table 2). The second introduces an area weighted average of the ice and open water stability dependent drag coefficients using the lead fraction (CLEAD). The third experiment applies a correction factor for low ice concentrations based on Overland's (1985) observation that the outer marginal ice zone is characterized by low ice concentrations and increased ice rafting which result in an increased surface drag (CRAFT).

The basic stability dependent formulation CSTAB produces drag coefficients which range from as low as 1.5×10^{-3} and as high as 4×10^{-3}, thus producing a similar range to those observed. The correction for ice concentration CLEAD shows a small decrease in the drag coefficient due to the decreased drag over open water surfaces compared to ice surfaces. The correction for rafting CRAFT also shows a very small change in the drag coefficient with slight increases over the polynya area. The CLEAD and CRAFT experiments produce such small changes in the simulation of the polynya compared to the introduction of the stability dependent formulation itself that we will confine much of our discussion to the CSTAB experiment.

Fig. 9 shows the simulated ice concentration and surface temperature for the 25 February, as well as the 3-day ice drift for the period 24 to 27 February, for the CSTAB experiment. Like the control experiment, the polynya has opened rapidly, but the extent is reduced to 84 km south from St. Lawrence Island. Further, in this simulation, the smaller scale structure of wind driven bands of ice is now apparent, also an improvement over the control experiment. These bands are due to the feedback effects between the drag coefficient and stability causing differential ice divergence, which in turn affects the stability. The scale of these bands is larger than those observed because

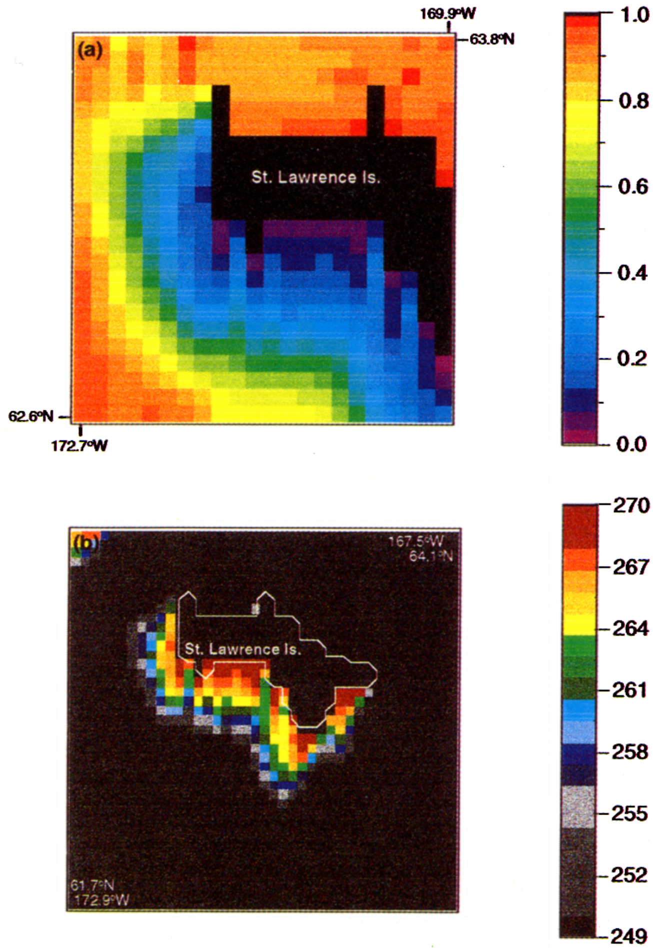

Fig. 9. CSTAB experiment: (a) Simulated ice concentration as a % for 00GMT 25 February 1992, for sub-sampled area of model domain to correspond with SAR data in Fig. 4. Pixel size is 7 km × 7 km. (b) Simulated surface temperature in °K (weighted average of ice and ocean temperatures) for 18GMT 24 February 1992, for sub-sampled area of model domain to correspond with AVHRR data in Fig. 5(c). Pixel size is 7 km × 7 km.

of the limited resolution of the ice model, and because there are additional, oceanic mechanisms likely to be operating in the real SLIP event. The simulated surface temperature shows that the first-year ice is still much too cold, but the increased ice concentration in the polynya allows the surface temperature to be much closer to the AVHRR data than the control. The remaining errors are due to the following factors: (i) the simple treatment of ice thermodynamics, with only two layers, no multiple ice types and a linear profile through the ice; (ii) a constant specified ocean heat flux rather than an ocean mixed layer model to calculate an interactive ocean heat flux; (iii) the minimum ice thickness of 30 cm, restricting the representation of new and thin ice; and (iv) inadequacies in the atmospheric radiative transfer treatment. All of these factors are being addressed in current and planned model development, and could not be part of this study. It was found that the changes in the surface drag coefficient and the resulting simulation for the CLEAD and CRAFT experiments were insignificant, and hence these results will not be presented, although polynya

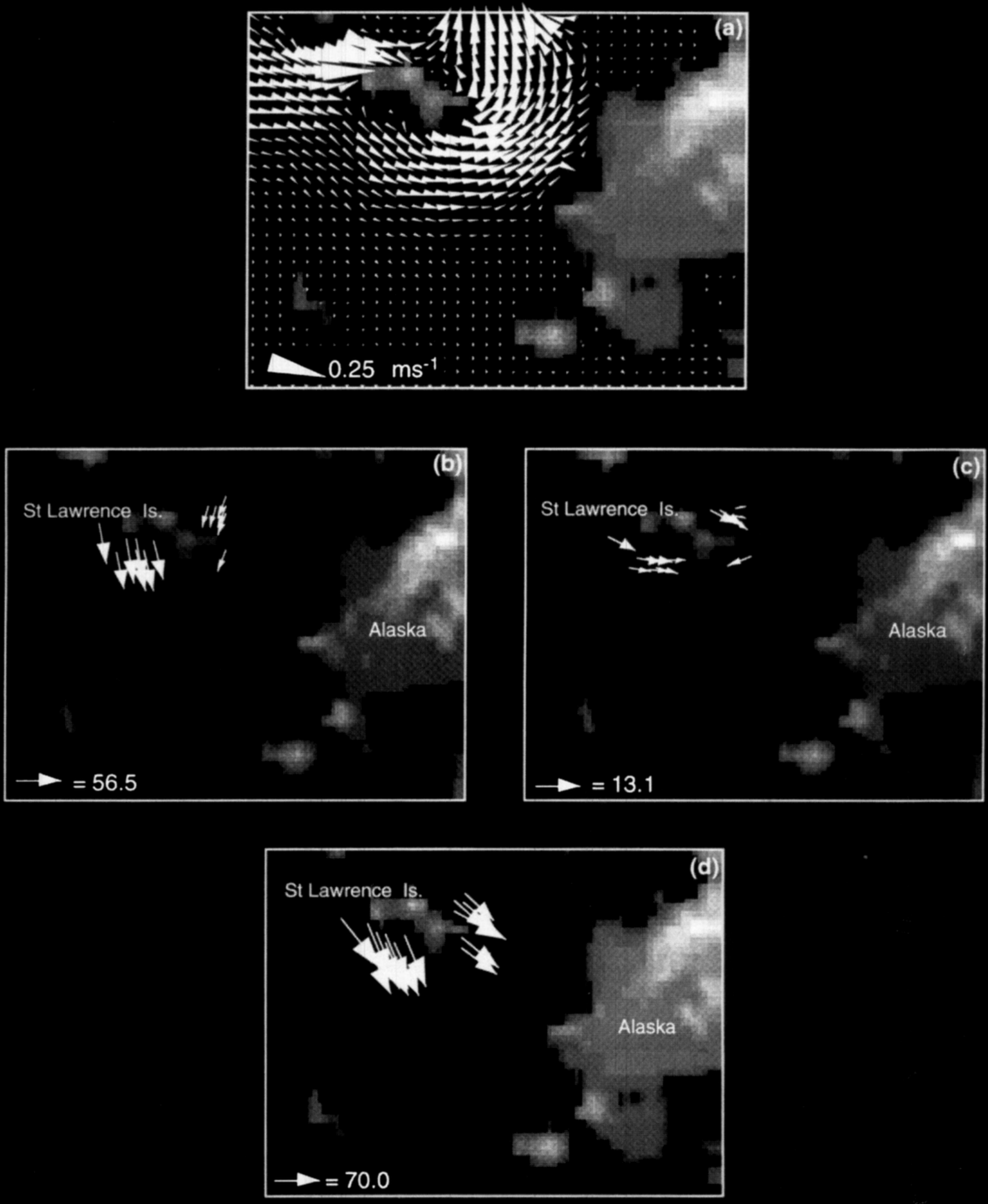

Fig. 10. (a) Ocean currents calculated for the region by the barotropic ocean model. Ice drift vectors (km in three days), for the period 27 February to 1 March, (b) derived from SAR imagery; (c) as simulated by the model without ocean currents and (d) as simulated by the model with ocean currents.

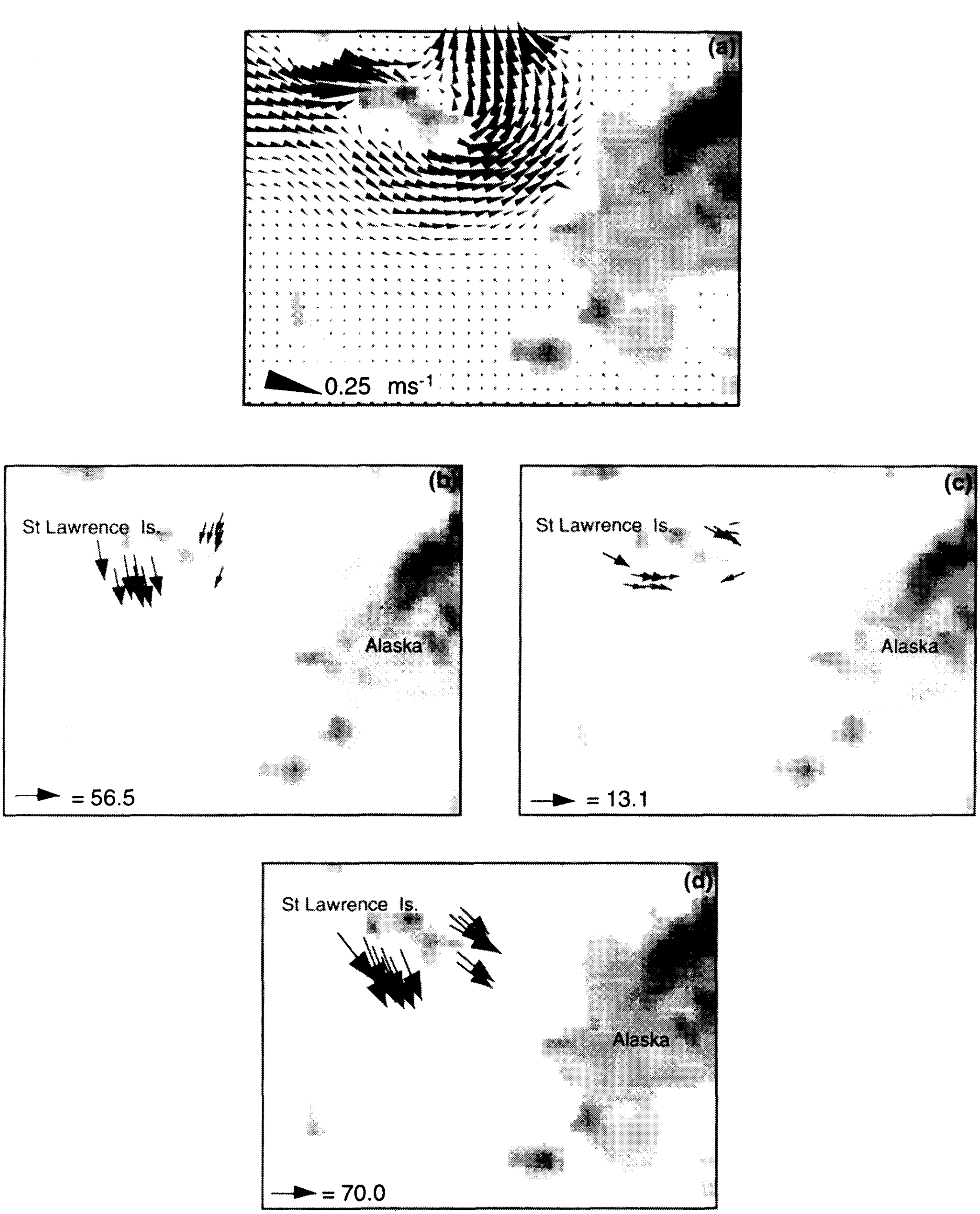

Fig. 10. (a) Ocean currents calculated for the region by the barotropic ocean model. Ice drift vectors (km in three days), for the period 27 February to 1 March, (b) derived from SAR imagery; (c) as simulated by the model without ocean currents and (d) as simulated by the model with ocean currents.

The simulated ice concentration and surface temperature for the 25 February are shown in Fig. 11. One of the most notable differences between the simulations with and without ocean circulation is the shape of the polynya region itself. The ocean run resulted in a polynya with more small scale structure resembling the north-south oriented band of ice observed in the SAR imagery, and a more gradual decrease in temperature from the coastline south to the seasonal ice pack. The area of low ice concentration located along the western coast of the island in the no-ocean simulation has been significantly reduced. All of these new characteristics are confirmed by the AVHRR and SAR imagery shown in Figs. 4, 5. The areal extent of the simulated polynya region is reduced compared to the no-ocean simulation and is similar to that evident in the imagery (Table 2). The impact of an imposed, idealized ocean circulation is greatest when the wind forcing is weak or variable. It is clear that a realistic and interactive ocean circulation is necessary for accurate simulation of ice drift, and it will be necessary to reckon with the lack of data regarding ice-ocean drag coefficients.

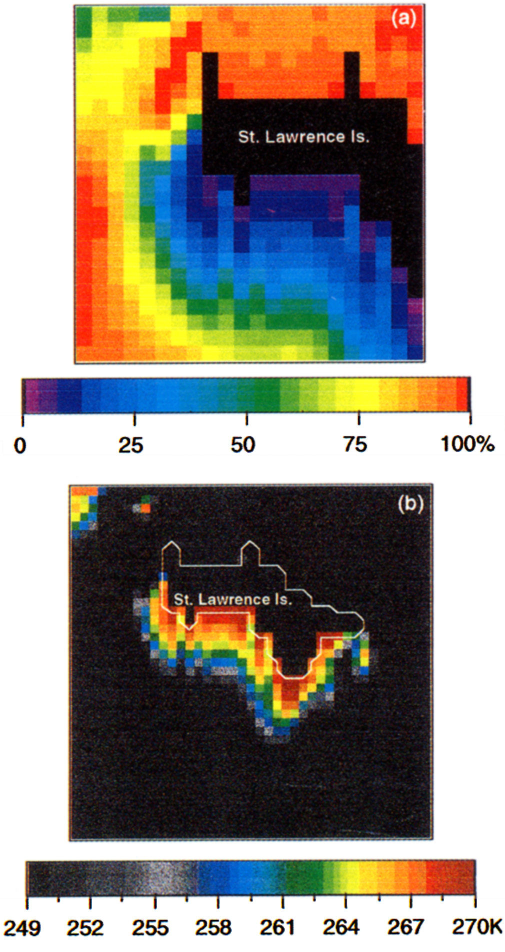

Fig. 11. (a) Simulated ice concentration in the experiment with ocean currents as a fraction for 00GMT 25 February 1992, for sub-sampled area of model domain to correspond with SAR data in Fig. 4. Pixel size is 7 km × 7 km. (b) Simulated surface temperature (°K) in the experiment with ocean currents (weighted average of ice and ocean temperatures) for 18 GMT 24 February 1992, for sub-sampled area of model domain to correspond with AVHRR data in Fig. 5. Pixel size is 7 km × 7 km.

7. Summary

Climate model simulations of high latitudes will need to account for the effects of large polynyas that form frequently on the lee side of coastlines. The results described here illustrate the interplay between high resolution modeling and satellite data in a study of a lee-side polynya adjacent to one of the Bering Sea's major islands. While validation of satellite data in this region is difficult, due to the scarcity of in situ observations, it nevertheless provides a valuable means of comparison with the model simulation.

The SAR provided ice motion products that, for the first time, have been used to verify a climate system model. This validation data revealed that the model's ice velocities responded too rapidly to changes in wind forcing, at least in the absence of ocean currents. The AVHRR data showed that the model's surface temperature gradients were too steep, pointing to a need for a more sophisticated treatment of ice and ocean thermodynamics. Further, the model provided unique information on several aspects of the polynya formation process, including the vertical extent and horizontal scale of the polynya's impact on the atmosphere and quantitative assessments of the impacts of the ocean surface currents and air-ice drag coefficients. The AVHRR data provided evidence that the reformulation of the drag coefficient improved the model simulation of surface temperature. The SAR imagery provided evidence of wind driven bands of frazil ice, which also contributed to the conclusion that feedbacks between atmospheric stability, ice concentration and the drag coefficient has an impact on the accurate simulation of sea ice in a climate model. Using the satellite data, the simulations were shown to have been improved by the inclusion of the physical processes dictated by the hypotheses.

The use of satellite imagery of the polynya event has identified key areas for improvement which will be necessary for the routine, accurate simulation of such phenomena. While some of these improvements are clearly related to the simulation of sea ice, other improvements in the model system and in data acquisition have been identified. Work on cloud-radiation interactions and the ocean formulation in the model are ongoing. For rigorous, quantitative model validation, more work on satellite data validation is required, and additional products for both comparison with model output and for model initialization is needed. Crucial products are sea ice thickness and snow thickness over sea ice.

The synergy between remotely sensed data and physically based models will be increasingly important as system models are applied to the polar regions. Because in situ measurements are particularly scarce over the sub-polar oceans, satellite observations will need to continue to guide model development. Models, in turn, will not only serve as vehicles for testing and improving our understanding of the polar system, but they will provide the predictive capability needed to assess possible changes over the coming decades. While global models will continue to be used to study large scale interactions and changes, high resolution regional models such as ARCSyM will provide the opportunity to simulate smaller scale processes, such as polynya formation, thereby guiding the parameterization of these processes and their effects in global models.

8. Acknowledgments

This work was supported by NASA's Polar Ocean Science Program through Grants NAGW-2829, NAGW-2637 and NAGW-2517 to the Geophysical Institute and the Institute of Marine Science, University of Alaska, at which the bulk of this work was performed. Computer time was supplied by the Arctic Region Supercomputing Center at the University of Alaska Fairbanks. SAR and AVHRR image processing was accomplished at the IIAS Lab of UAF Geophysical Institute with training provided by Joanne Groves and Rick Guritz. Details of image processing and analyses as well as GPS ice motion analyses will be available in a University of Alaska Fairbanks dissertation written by Mary F. Glueck. We gratefully acknowledge the assistance of Jim Maslanik and Chuck Fowler in supplying the SSM/I data. Ron Kwok and members of the SAR Systems Development and Processing Group at JPL provided much appreciated assistance with SAR ice motion processing and analyses.

REFERENCES

Aagaard, K., Coachman, L. K. and Carmack, E. 1981. On the halocline of the Arctic Ocean. *Deep Sea Res.* **28**, 529–545.

Anthes, R. A., Hsie, E. Y. and Kuo, Y. H. 1987. Description of the Penn State/NCAR Mesoscale Model Version 4 (MM4). *NCAR Tech Note*, NCAR/TN-282+STR, 66 pp.

Briegleb, B. P. 1992a. Delta-Eddington approximation for solar radiation in the NCAR Community Climate Model. *J. Geophys. Res.* **97**, 7603–7612.

Briegleb, B. P. 1992b. Long-wave band model for thermal radiation in climate studies. *J. Geophys. Res.* **97**, 11,475–11,485.

Carsey, F. D. 1989. Review and status of remote sensing of sea ice. *IEEE J. Ocean. Eng.* **14**, 127–138.

Carsey, F. D. (ed.) 1992. Microwave remote sensing of sea ice. *Geophysical Monograph* **68**, American Geophysical Union, Washington, D.C., 462 pp.

Cavalieri, D. J. 1983. MIZEX West: Bering Sea Marginal Ice Zone Experiment. *Eos. Trans. AGU* **64**, 578–580.

Cavalieri, D. J., Gloersen P. and Campbell, W. J. 1984. Determination of sea ice parameters with the Nimbus 7 SMMR. *J. Geophys. Res.* **89**, 5355–5369.

Cavalieri, D. J., Crawford, J. P., Drinkwater, M. R., Eppler, D. T., Farmer, L. D., Jentz, R. R. and Wackerman, C. C. 1991. Aircraft active and passive microwave validation of sea ice concentration from the defense meteorological satellite program special sensor microwave imager. *J. Geophys. Res.* **96**, 21989–22008.

Cavalieri, D. J. and Onstott, R. G. 1992. Arctic coastal polynya observations with ERS-1 SAR and DMSP

SSM/I. *Proc. First ERS-1 Symposium: Space at the service of our environment.* Cannes, France, 4–6 November 1992, pp. 295–299.

Coachman, L. K., Aagaard, K. and Tripp, R. B. 1975. *Bering Strait: The regional physical oceanography.* University of Washington Press, Seattle, 172 pp.

Curlander, J. C., Holt, B. and Hussey, K. J. 1985. Determination of sea ice motion using digital SAR imagery. *IEEE J. Oceanic Engineering,* **OE-10**, 358–367.

Curry, J. A. and Ebert, E. E. 1992. Annual cycle of radiation fluxes over the Arctic Ocean: sensitivity to cloud optical properties. *J. Climate* **5**, 1267–1280.

Deardorff, J. W. 1968. Dependence of air-sea transfer coefficients on bulk stability. *J. Geophys. Res.* **73**, 2549–2557.

DeSoto, Y., Tippens, H., Kotlarek, T. and Hsu, I. 1991. *User's guide, Alaska SAR facility archive and catalog subsystem.* **JPL D-5496**, NASA Jet Propulsion Lab, Pasadena, CA, 145 pp.

Dickinson, R. E., Henderson-Sellers A. and Kennedy, P. J. 1993. Biosphere-Atmosphere transfer scheme (BATS) version 1E as coupled to the NCAR community climate model. *NCAR Tech Note,* **NCAR/TN-387+STR**, 72 pp.

Flato, G. M. and Hibler III, W. D. 1992. Modeling pack ice as a cavitating fluid. *J. Phys. Oceanogr.* **22**, 626–651.

Giorgi, F., Marinucci, M. R. and Bates, G. T. 1993a: Development of a second generation regional climate model (RegCM2). Part I: Boundary layer and radiative transfer processes. Mon.Wea.Rev., **121**, 2794–2813.

Giorgi, F., Marinucci, M. R., Bates, G. T. and de Canio, G. 1993b. Development of a second generation regional climate model (RegCM2). Part II: Convective processes and assimilation of lateral boundary conditions. *Mon. Wea. Rev.* **121**, 2814–2832.

Gloersen, P. and Cavalieri, D. J. 1986. Reduction of weather effects in the calculation of sea ice concentration from microwave radiance. *J. Geophys. Res.* **91**, 3913–3919.

Gloersen, P., Campbell, W. J., Cavalieri, D. J., Comiso, J. C., Parkinson, C. L. and Zwally, H. J. 1992. *Arctic and Antarctic sea ice, 1978–1987: satellite passive microwave observations and analysis.* **NASA SP-511**, 290 pp.

Grell, G. A. 1993. Prognostic evaluation of assumptions used by cumulus parameterizations. *Mon. Wea. Rev.* **121**, 764–787.

Haefliger, M., Steffen, K. and Fowler, C. 1993. AVHRR surface temperature and narrow band albedo comparison with ground measurements for the Greenland ice sheet. *Ann. Glaciol.* **17**, 49-54.

Holtslag, A. A. M., de Bruijn, E. I. F. and Pan, H. L. 1990. A high resolution air mass transformation model for short range weather forecasting. *Mon. Wea. Rev.* **118**, 1561–1575.

Hsie, E. Y., Anthes, R. A. and Keyser, D. 1984. Numerical simulation of frontogenesis in a moist atmosphere. *J. Atmos. Sci.* **41**, 2581–2594.

Johannessen, O. M. and Horn, D. A. 1984: MIZEX 84: A brief overview. *MIZEX Bull.* **5**, 1–7, Cold. Reg. Res. and Eng. Lab., Hanover, N.H., USA.

Key, J. and Haefliger, M. 1992. Arctic ice surface temperature retrieval from AVHRR thermal channels. *J. Geophys. Res.* **97**, 5885–5893.

Kwok, R. and Cunningham, G. 1993. *Alaska SAR facility geophysical processor system data user's handbook, version 2.0.* **JPL D-9526**, NASA Jet Propulsion Lab, Pasadena, CA, 150 pp.

Kwok, R., Rignot, E., Holt, B. and Onstott, R. 1991. An overview of the geophysical sea ice products generated at the Alaska SAR Facility. *J. Geophys. Res.* **97**, 2391–2402.

Lynch, A. H., Chapman, W., Walsh, J.E. and Weller, G. 1995. Development of a regional climate model of the western Arctic. *J. Climate* **8**, 1555–1570.

Macklin, S. A. 1983. Wind drag coefficient over first-year sea ice in the Bering Sea. *J. Geophys. Res.* **88**, 2845–2852.

Martin, S. and Cavalieri, D. J. 1989. Contributions of the Siberian shelf polynyas to the Arctic Ocean intermediate and deep water. *J. Geophys. Res.* **94**, 12,725–12,738.

Maslanik, J. and Key, J. 1993. Comparison and integration of ice pack temperatures derived from AVHRR and passive microwave imagery. *Ann. Glaciol.* **17**, 372–378.

Massom, R. and Comiso, J. C. 1994. The classification of Arctic sea ice types and the determination of surface temperature using advanced very high resolution radiometer data. *J. Geophys. Res.* **99**, 5201–5218.

Maykut, G. A. 1982. Large-scale heat exchange and ice production in the central Arctic. *J. Geophys. Res.* **87**, 7971–7984.

McCandless, S. W., Jr. and Mango, S. A. 1990. *The theory, design and application of space based synthetic aperture radar, vols 1 and 2.* Lectures from a short course given at the Alaska SAR Facility, Geophysical Institute, University of Alaska Fairbanks, Alaska, November 1990, 634 pp.

McMillan, L. M. and Crosby, D. B. 1984. Theory and validation of the multiple window sea surface temperature technique. *J. Geophys. Res.* **89**, 3655–3661.

McNutt, L. 1981. Ice conditions in the eastern Bering Sea from NOAA and Landsat imagery: Winter conditions 1974, 1975, 1976, 1979. *NOAA Tech. Memo.* **ERL PMEL-24**, NOAA Pacific Marine Environmental Laboratory, Seattle, WA, 179 pp.

Niebauer, H. J. 1980. Sea ice and temperature variability in the eastern Bering Sea and the relation to atmospheric fluctuations. *J. Geophys. Res.* **85**, 7507–7515.

NSDIC, 1992: *DMSP SSM/I brightness temperature grids for the polar regions on CD-ROM: user's guide.* NSDIC, **Special Report-1**, Boulder, January 1992.

Overland, J. E. 1985. Atmospheric boundary layer structure and drag coefficients over sea ice. *J. Geophys. Res.* **90**, 9029–9049.

Overland, J. E. and Pease, C. H. 1982. Cyclone climatology of the Bering Sea and its relation to sea ice extent. *Mon. Wea. Rev.* **110**, 5–13.

Overland, J. E. and Roach, A. T. 1987. Northward flow in the Bering and Chukchi Seas. *J. Geophys. Res.* **92**, 7097–7105.

Parkinson, C. L. and Washington, W. M. 1979. A large-scale numerical model of sea ice. *J. Geophys. Res.* **84**, 311–337.

Pease, C. H. 1987. The size of wind-driven coastal polynyas. *J. Geophys. Res.* **92**, 7049–7059.

Pease, C. H. 1980. Eastern Bering Sea ice processes. *Mon. Wea. Rev.* **108**, 2015–2023.

Proshutinsky, A. Yu. 1988. Modeling seasonal fluctuations of the level of the Arctic Ocean. *Soviet Meteorology and Hydrology.* **2**, 39–46.

Schumacher, J. D., Aagaard, K., Pease, C. H. and Tripp, R. B. 1983. Effects of a shelf polynya on flow and water properties in the northern Bering Sea. *J. Geophys. Res.* **88**, 2723–2732.

Shea, D. J., Trenberth, K. E. and Reynolds, R. W. 1992. A global monthly sea surface temperature climatology. *J. Climate* **5**, 987–1001.

Thorndike, A. S. and Colony, R. 1982. Sea ice motion in response to geostrophic winds. *J. Geophys. Res.* **87**, 5845–5852.

Trenberth, K. E., 1992. Global analyses from ECMWF and atlas of 1000mb to 10mb circulation statistics. *NCAR Tech Note,* **NCAR/TN-373+STR**, 191 pp.

Ulaby, F. T., Moore, R. K. and Fung, A. K. 1981. *Microwave remote sensing: active and passive, vol I: fundamentals and radiometry.* Addison-Wesley, Reading, Mass., 2162 pp.

Untersteiner, N. 1980. AIDJEX Review. *Sea ice processes and models.* R. S. Pritchard (ed.). University of Washington Press, Seattle, Washington, 3–11.